

Gas Permeability Change with Deformation and Cracking of a Sandstone under Triaxial Compression

Yuan-Jian LIN

China University of Mining and Technology

Jiang-Feng LIU (✉ jeafliu@hotmail.com)

China University of Mining and Technology <https://orcid.org/0000-0002-4847-7102>

Tao CHEN

Sinopec Shengli Oilfield

Shi-Jia MA

China University of Mining and Technology

Pei-Lin WANG

China University of Mining and Technology

Hai-Bo BAI

China University of Mining and Technology

Research Article

Keywords: sandstone, gas permeability, micro-pore/fracture structure, confining pressure, gas pressure

Posted Date: April 29th, 2021

DOI: <https://doi.org/10.21203/rs.3.rs-392045/v1>

License: © ⓘ This work is licensed under a Creative Commons Attribution 4.0 International License.

[Read Full License](#)

Abstract

In this paper, a THMC multi-field coupling triaxial cell was used to systematically study the evolution of gas permeability and the deformation characteristics of sandstone. The effects of confining pressure, axial pressure and air pressure on gas permeability characteristics were fully considered in the test. The gas permeability of sandstone decreases with increasing confining pressure. When the confining pressure is low, the variation of gas permeability is greater than the variation of gas permeability at high confining pressure. The gas injection pressure has a significant effect on the gas permeability evolution of sandstone. As the gas injection pressure increases, the gas permeability of sandstone tends to decrease. At the same confining pressure, the gas permeability of the sample during the unloading path is less than the gas permeability of the sample in the loading path. When axial pressure is applied, the axial stress has a significant influence on the permeability evolution of sandstone. When the axial pressure is less than 30 MPa, the gas permeability of the sandstone increases as the axial pressure increases. At axial pressures greater than 30 MPa, the permeability decreases as the axial pressure increases. Finally, the micro-pore/fracture structure of the sample after the gas permeability test was observed using 3D X-ray CT imaging.

1 Introduction

Compared with oil and coal, natural gas is considered to be a cleaner and more efficient energy source. Unconventional resources, such as tight sandstone gas, are at the bottom of the global natural gas resource pyramid, although its potential resources are considerably greater than the reserves of conventional natural gas (Khlaifat et al., 2011). At present, although the research on tight sandstone gas is still in the initial stages, its reserves are large, and the recoverable reserves are approximately 1/3 of the total amount of natural gas. Sandstone gas is a typical unconventional natural gas resource that is stored in low-permeability or ultra-low-permeability tight sandstone reservoirs. Sandstone gas is difficult to mine by conventional techniques. Therefore, it is usually necessary to produce natural gas of economic value through large-scale fracturing or special gas recovery process technology (Fig. 1). Reservoir porosity and permeability are two important parameters for reservoir evaluation (Wang et al., 2017a; Xiao et al., 2017; Yang and Huang, 2020). In particular, the stress sensitivity of gas permeability has a strong impact on the mining effect of low permeability tight oil and gas fields.

In recent years, extensive research has been conducted on the gas permeability characteristics of sandstone (Amann-Hildenbrand et al., 2016; Duan et al., 2014; Fu et al., 2015; Ghanbarian et al., 2016; Wang et al., 2017b; Zhang et al., 2019). Results indicate that the reduction in the effective permeability of the gas is primarily caused by the crack closure as a result of the increase in the confining pressure under the condition of constant water content. In addition, studies have also found that some samples even have a large dispersion of initial effective permeability. However, there is a confining pressure-saturation threshold, and when this threshold is exceeded, the gas effective permeability of the samples decreases abruptly (Duan et al., 2014; Fu et al., 2015; Wang et al., 2017b). However, these studies have neglected the evolution of gas permeability after sample fracture. In mining, the gas permeability of sandstone after

fracturing is a highly important parameter that cannot be ignored. In addition, the microscopic pore structure after fracturing is of great significance for evaluating the mesoscopic mechanism of gas migration. At present, there is little research on this aspect.

In this paper, we focused on the evolution of gas permeability during cyclic loading and unloading and considered the effect of air pressure on gas permeability characteristics. Furthermore, we also studied the evolution law of gas permeation of sandstone during fracturing and reconstructed the fractured specimen by CT scanning to observe the internal pore fracture structure.

2 Materials And Methods

2.1 Materials and experimental scheme

The samples were obtained from a field in Anhui Province, China. The samples were prepared as cylinders 50 mm in diameter and 20 mm in length. Two samples were first placed into a triaxial cell to perform gas permeability tests. At the end of the test, one of the specimens was sent for three-dimensional CT scanning to observe the internal cracks.

Confining pressure was applied from 1 MPa until 20 MPa. Different air pressures were applied at different confining pressure stages. The purpose was to study the barometric sensitivity of permeability. In the first phase, the confining pressure is loaded and unloaded in a stepwise manner. To consider the complexity of the stress on the sand in the field, we performed two cycles of loading and unloading. In the second stage, the confining pressure was restored to 20 MPa, and axial pressure was applied. The axial pressure was applied from 5 MPa with stepwise loading (loading gradient of 5 MPa) until the sample was fractured. The gas pressure was maintained at 0.5 MPa throughout the loading process. The flow chart of the experimental scheme is shown in Fig. 2.

2.2 Gas permeability calculation method

The permeability calculation was performed using the steady-state method, which works well for samples with a permeability higher than 10^{-19} m^2 and has been used widely in many studies (Liu et al., 2020; Liu et al., 2015). This study also applied this method combined with our own gas permeability test device (Fig. 3). The confining pressure is controlled by the servo system. The gas is inert (argon) and is injected into a fixed volume cylinder (0.4 ml) from the gas source. The gas is later injected into a triaxial pressure chamber at a given pressure P_1 , and the gas pressure drop ΔP is recorded over time Δt . The average pressure (P_{mean}) in the cylinder during Δt is $P_{\text{mean}} = P_1 - \Delta P/2$. According to Darcy's law, the formula for calculating the effective gas permeability (k_{eff}) is

$$k_{\text{eff}} = \frac{\mu_g V_0}{A} \frac{2h\Delta P}{(P_{\text{mean}}^2 - P_0^2)\Delta t} \quad (1)$$

where μ_g is the dynamic viscosity of the fluid ($2.2 \times 10^5 \text{ Pa} \cdot \text{s}$), V_0 is the volume of the buffer reservoir, h is the sample height, and A is the cross-sectional area of the sample.

2.3 Klinkenberg (or slip) effect

The Klinkenberg (or slip) effect refers to the phenomenon where the gas exhibits a finite velocity on the solid wall and the velocity of the liquid is zero when the gas moves through the porous medium. This phenomenon exhibited by the gas is known as the slip or the Klinkenberg effect^[116]:

$$k_{\text{eff}} = k_{\infty} \left(1 + \frac{4cl}{r} \right) = k_{\infty} \left(1 + \frac{b}{P} \right)$$

2

where k_{∞} is the intrinsic permeability; l is the mean free path of the gas molecule; r is the average radius of the pore; c is the scale factor; b is the Klinkenberg coefficient or the slip factor, and P is the pore pressure. The slip factor is defined as

$$b = \frac{c\kappa T}{\sqrt{2}\pi r^3}$$

3

where κ is the Boltzmann constant, and T is the absolute temperature.

2.4 Micro-CT observation test

The three-dimensional scan was tested in Advanced Analysis & Computation Center, China University of Mining and Technology. The test instrument is Carl Zeiss Xradia 510 Versa High Solution 3D X-ray Microanalyser, with a 3D spatial resolution: $55\mu\text{m}$ - $0.5\mu\text{m}$. In order to observe the macroscopic crack of the rock sample, the observation was performed after the triaxial compression test.

3 Results And Discussion

3.1 Effect of loading/unloading on gas permeability

Figures 4(a) ~ (b) shows the evolution of gas permeability of two samples (C1 and C2) under different confining pressures. To avoid the interference of air pressure on the permeability results, we only plotted the gas permeability results with a pressure of 0.5 MPa. Gas permeability was decreased by one order of magnitude (from $1.48 \times 10^{-15} \text{ m}^2$ to $1.39 \times 10^{-16} \text{ m}^2$) for sample C1 and 3.3 times (from $5.0 \times 10^{-16} \text{ m}^2$ to $1.50 \times 10^{-16} \text{ m}^2$) for sample C2 throughout the experiment. The gas permeability decreases with increasing confining pressure. When the confining pressure is less than 5 MPa, gas permeability decreases rapidly: 7.59 times for sample C1 and 2.27 times for C2(0→5MPa). When the confining

pressure is greater than 5 MPa, the rate of decrease of gas permeability gradually reduces: 1.40 times for sample C-1 and 1.66 times for C2(5→20MPa). When considering the explanation for this phenomenon, there are some large pores inside the sample at the initial stage. As the confining pressure increases, this part of the pores closes rapidly, resulting in a decrease in permeability accumulation. As the confining pressure continues to increase, the remaining pores are less sensitive to the confining pressure. Therefore, the change in confining pressure has a small effect on the permeability.

For unloading stage: 20→5 MPa, the gas permeability difference between unloading stage and loading stage under the same confining pressure is small (e.g., sample C1: $1.50 \times 10^{-16} \text{ m}^2$ (unloading-10MPa) vs. $1.62 \times 10^{-16} \text{ m}^2$ (loading-10MPa)). When the confining pressure is decreased from 5 MPa to 1 MPa, the hysteresis effect of the permeability is obvious. The permeability corresponding to the unloading stage under the same confining pressure is much smaller than the permeability corresponding to the loading stage (e.g., sample C1: $5.51 \times 10^{-16} \text{ m}^2$ (unloading-1MPa) vs. $14.81 \times 10^{-16} \text{ m}^2$ (loading-1MPa)).

For the second cycle of loading and unloading, the test results in the loading phase are mostly the same as the results in the unloading phase of the first cycle. During the unloading phase, there is still little change in gas permeability (compared to results from other phases under the same confining pressure). When the confining pressure returned to the initial value (1 MPa), the gas permeability was slightly less than the loading phase (sample C1: $5.51 \times 10^{-16} \text{ m}^2$ vs. $4.07 \times 10^{-16} \text{ m}^2$). Compared with the loading phase results of the first cycle, the gas permeability decreased from $14.81 \times 10^{-16} \text{ m}^2$ to $4.07 \times 10^{-16} \text{ m}^2$. This indicates that some of the pores cannot be opened after they are closed, although the confining pressure returns to the initial state. Similar trend was found for sample C2.

Figure 4(b) shows the deformation characteristics of the sample during the gas permeability test. In general, the deformation law follows the evolution law of gas permeability. Similarly, when the confining pressure is less than 5 MPa, the deformation of the sample is large. Above 5 MPa, the deformation of the sample is less sensitive to the confining pressure. In the second loading and unloading cycle, the deformation of the sample is mainly in the elastic range, and some deformation is unrecoverable compared with the first cycle.

3.2 Effect of gas pressure on gas permeability

Figure 5(a) and (b) show the effect of gas pressure on gas permeability during the first and second loading-unloading cycles. First, the gas permeability decreases with increasing gas pressure at the same confining pressure. This phenomenon can be attributed to the Klinkenberg effect. At lower gas pressures (less than 1 MPa), gas permeability is relatively more sensitive to gas pressure. There is no significant difference in the gas pressure sensitivity of gas permeability under different confining pressures. In the second cycle of loading and unloading, the effect of gas pressure on permeability is largely similar to that of the first cycle. Furthermore, the gas permeability at low pressure is more sensitive to the gas pressure. When the gas pressure exceeds 2 MPa, the change in gas pressure has little effect on the gas permeability.

3.3 Effect of loading pressure on gas permeability

Figure 5(b) shows the deformation characteristics of the specimen during the application of the axial pressure. Similar to the law of change of permeability, when the confining pressure is less than 5 MPa, there is little deformation of the sample. When the axial pressure is greater than 5 MPa, the deformation of the sample gradually increases as the axial pressure increases. However, when the axial pressure is greater than 20 MPa, the deformation of the sample decreases as the axial pressure increases. This phenomenon is difficult to explain and we will verify it in subsequent trials.

3.4 Micro-pore/fracture structure

3.4.1 3D pore-fracture structure reconstruction

After the gas permeability test, the sample C1 was scanned using 3D X-ray Microanalyser. The image resolution was 53.14 μm , which was scanned a layer at a time from top to bottom. After the scanning was completed, the slices were three-dimensionally reconstructed by a compiled algorithm to obtain a three-dimensional reconstruction model of the sample. As shown in Fig. 6, there is a macroscopic crack in the height direction at an angle of 45° degree. In addition, when observing the cross-section, the crack primarily exists at the edge of the cross-section.

Figure 7 shows the evolution of the crack generation and permeability. Phase I: in the initial stage, the stress on the pore structure of the sample is weak due to the small axial pressure. Therefore, the permeability remains largely unchanged. Phase II: as the axial pressure increases, micro-cracks begin to form inside the sample and the gas permeability begins to increase gradually. When a crack is generated at an angle of 45° degree in the height direction, the gas permeability is maximized. Phase III: as the axial pressure continues to increase, the axial pressure will compress the crack, resulting in a decrease in permeability. Therefore, the evolution of permeability during the complete process varies as follows: stable→slowly increasing→reaching peak→gradually decreasing.

3.4.2 Quantitative characterization of pore (crack) structure

To quantitatively characterize the pore structure of the sample, we separated the pore structure from the matrix as shown in Fig. 8(a). We also extracted its pore structure. The porosity was calculated as 7% by subsequent processing of the CT image. This result is less than the value (10%) measured by the nitrogen adsorption test. This is mainly due to the resolution of the CT, resulting in some of the smaller pores not being observed.

Because the isolated pore fracture does not contribute to the seepage characteristics, we extract the connected pores from all pores and calculate the pore connectivity:

$$L_C = \frac{V_C}{V_T} (4)$$

where L_C is the pore connectivity, V_C is the total volume of the connected pores, and V_T is the total pore volume. The calculated pore connectivity of the sample is 64.41%. According to 1(b), most of the connected pores are concentrated in half of the sample, while the isolated pores mainly exist in the upper left part. Therefore, the main migration path of gas during gas flow should be via macroscopic fractures and connected pores.

4 Conclusions

This study systematically examined the gas permeability of two sandstone samples under a couple effect of confining pressure, axial pressure and gas pressure. First, the influence of cyclic loading and unloading on the evolution of gas permeation was analysed. The evolution of the gas permeability occurred primarily in the first cycle of loading and unloading. Especially at the initial stage of loading (confining pressure less than 5 MPa), the gas permeability decreased by 7.59 and 2.27 times for samples C1 and C2, respectively. From 5 MPa to 20 MPa, the gas permeability decreased only a little. This means that most of the pores in the initial stage that allow the gas to flow have been closed, and subsequent pressurization has less effect on the deformation of the pore structure. After two cycles of loading and unloading, the gas permeability recovered to $4.07 \times 10^{-16} \text{ m}^2$ (C1) and $2.51 \times 10^{-16} \text{ m}^2$ (C2), which is fairly different from the initial value. This finding indicates that some of the pores have been plastically deformed and cannot be recovered.

When axial pressure is applied, the gas permeability gradually increases due to the expansion of the crack. When macroscopic cracks are generated, the permeability reaches a maximum. The axial pressure increased further and the permeability reduced due to the compaction of the axial pressure on the macro crack. Based on microscopic CT images, the cracks are mainly oriented at a 45° degree angle along the height direction. Further quantitative analysis revealed that the porosity was approximately 7%, which was relatively tight, and indirectly verified the phenomenon of low macroscopic gas permeability.

In addition, we also considered the Klinkenberg (gas slippage) effect and found that when the gas pressure exceeds 2 MPa, the change in gas pressure has little effect on the permeability. There is no significant difference in the gas slippage effect under different confining pressures, and the slippage effect in the loading stage is clearer than that in the unloading stage. Studies have also found that the slip factor tends to increase as the intrinsic permeability decreases. This phenomenon can be primarily attributed to the pore structure being subjected to pressure and causing the pore size to decrease. As a result, the frequency of collision between the gas molecules and the inner wall of the pores increases, resulting in a slip phenomenon of the gas and an increase in the slip factor.

Declarations

Acknowledgment

The authors are grateful to the support of the National Natural Science Foundation of China (No. 51809263), China Postdoctoral Science Foundation (2019M661993), and the Open Fund of MOE Key Laboratory of Deep Earth Science and Engineering (Sichuan University) (Grant No. DESE201906). The scanning service supported by Advanced Analysis & Computation Center, China University of Mining and Technology is also greatly acknowledged.

Declarations

Conflict of interest The authors declare that they have no conflict of interest.

References

- Amann-Hildenbrand, A., Dietrichs, J.P., Krooss, B.M., 2016. Effective gas permeability of Tight Gas Sandstones as a function of capillary pressure – a non-steady-state approach. *Geofluids* 16, 367-383.
- Duan, Q.B., Yang, X.S., 2014. Experimental studies on gas and water permeability of fault rocks from the rupture of the 2008 Wenchuan earthquake, China. *Science China Earth Sciences* 57, 2825-2834.
- Duan, Z., Davy, C.A., Agostini, F., Jeannin, L., Troadec, D., Skoczylas, F., 2014. Gas recovery potential of sandstones from tight gas reservoirs. *International Journal of Rock Mechanics & Mining Sciences* 65, 75-85.
- Environmental Protection Agency, O.o.R.a.D., 2015. Assessment of the Potential Impacts of Hydraulic Fracturing for Oil and Gas on Drinking Water Resources. External Review Draft.
- Fu, X., Agostini, F., Skoczylas, F., Jeannin, L., 2015. Experimental study of the stress dependence of the absolute and relative permeabilities of some tight gas sandstones. *International Journal of Rock Mechanics & Mining Sciences* 77, 36-43.
- Ghanbarian, B., Torresverdín, C., Skaggs, T.H., 2016. Quantifying tight-gas sandstone permeability via critical path analysis. *Advances in Water Resources* 92, 316-322.
- Khlaifat, A., Qutob, H., Barakat, N., 2011. Tight gas sands development is critical to future world energy resources, Society of Petroleum Engineers.
- Liu, J.-F., Ni, H.-Y., Cao, X.-L., Ma, L.-K., Guo, J.-N., Chen, X., 2020. Laboratory investigation on gas permeability of compacted GMZ bentonite under a coupled hydraulic-mechanical effect. *Engineering Geology* 276, 105761.
- Liu, J.F., Skoczylas, F., Talandier, J., 2015. Gas permeability of a compacted bentonite–sand mixture: coupled effects of water content, dry density, and confining pressure. *Canadian Geotechnical Journal* 52, 1159-1167.

Moghadam, A.A., Chalaturnyk, R., 2014. Expansion of the Klinkenberg's slippage equation to low permeability porous media. *International Journal of Coal Geology* 123, 2-9.

Tanikawa, W., Shimamoto, T., 2009. Comparison of Klinkenberg-corrected gas permeability and water permeability in sedimentary rocks. *International Journal of Rock Mechanics & Mining Sciences* 46, 229-238.

Wang, H.L., Xu, W.Y., Cai, M., Xiang, Z.P., Kong, Q., 2017a. Gas Permeability and Porosity Evolution of a Porous Sandstone Under Repeated Loading and Unloading Conditions. *Rock Mechanics & Rock Engineering* 50, 1-13.

Wang, Y., Agostini, F., Skoczylas, F., Jeannin, L., Portier, É., 2017b. Experimental study of the gas permeability and bulk modulus of tight sandstone and changes in its pore structure. *International Journal of Rock Mechanics & Mining Sciences* 91, 203-209.

Xiao, D., Lu, S., Yang, J., Zhang, L., Li, B., 2017. Classifying Multiscale Pores and Investigating Their Relationship with Porosity and Permeability in Tight Sandstone Gas Reservoirs. *Energy & Fuels* 31, 9188-9200.

Yang, D., Wang, W., Chen, W., Wang, S., Wang, X., 2017. Experimental investigation on the coupled effect of effective stress and gas slippage on the permeability of shale. *Scientific Reports* 7, 44696.

Yang, S.Q., Huang, Y.H., 2020. Effect of damage on gas seepage behavior of sandstone specimens. *Journal of Rock Mechanics and Geotechnical Engineering* 12, 866-876.

Zhang, H., Zhong, Y., Kuru, E., Kuang, J., She, J., 2019. Impacts of permeability stress sensitivity and aqueous phase trapping on the tight sandstone gas well productivity - A case study of the Daniudi gas field. *Journal of Petroleum Science and Engineering* 177, 261-269.

Figures

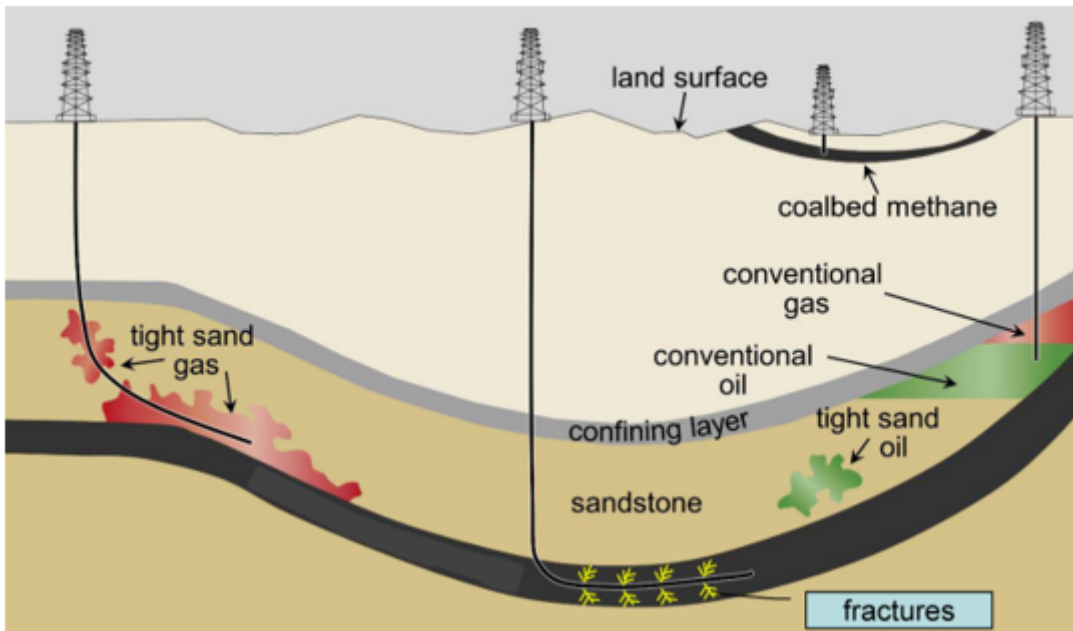


Figure 1

Schematic diagram of sandstone gas reservoirs(Environmental Protection Agency, 2015).

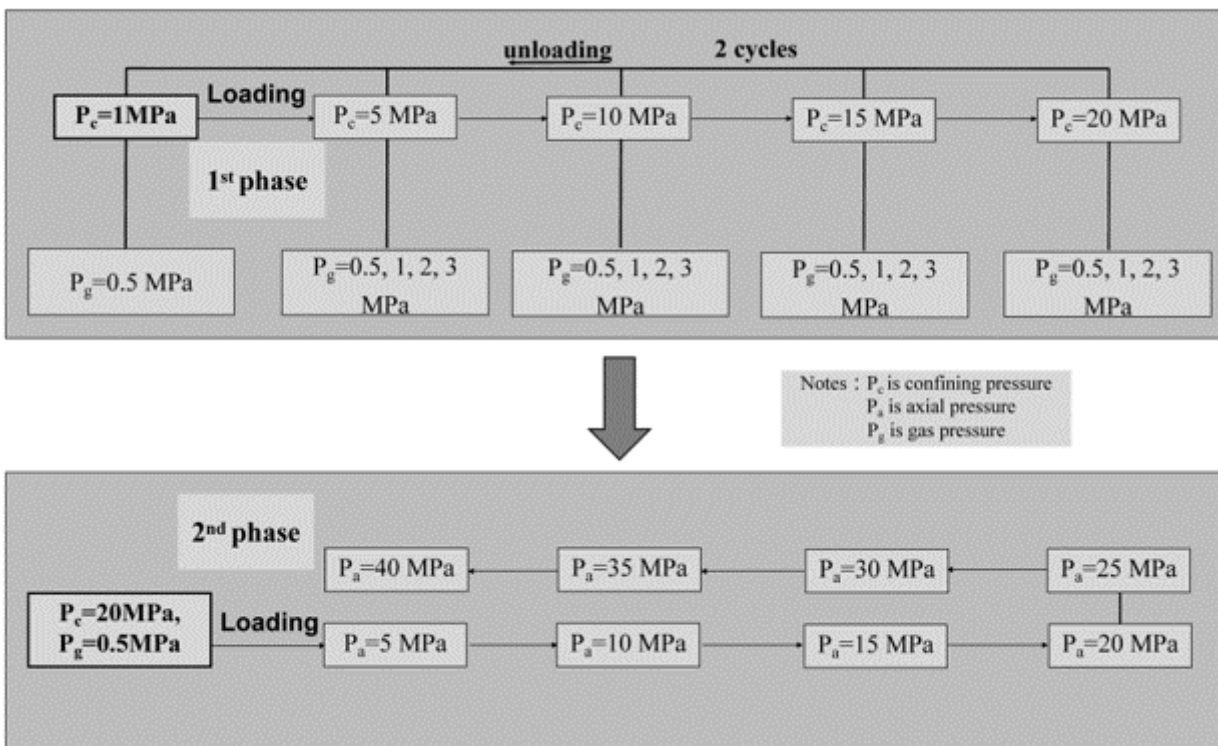


Figure 2

Experimental scheme.

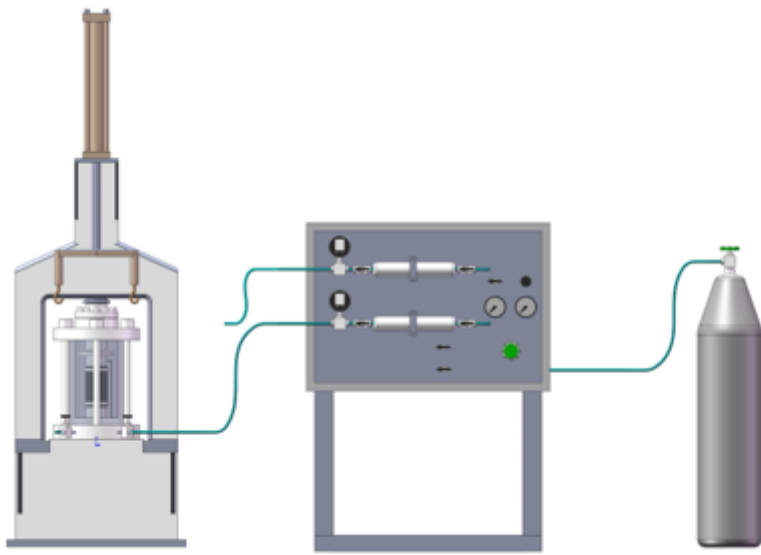


Figure 3

Gas permeability measurement devices(Liu et al., 2020).

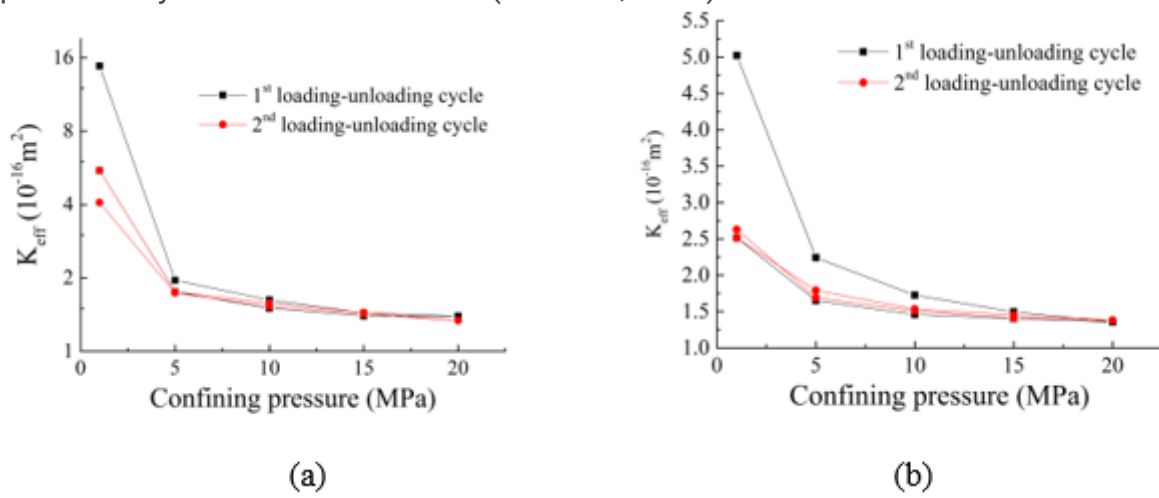
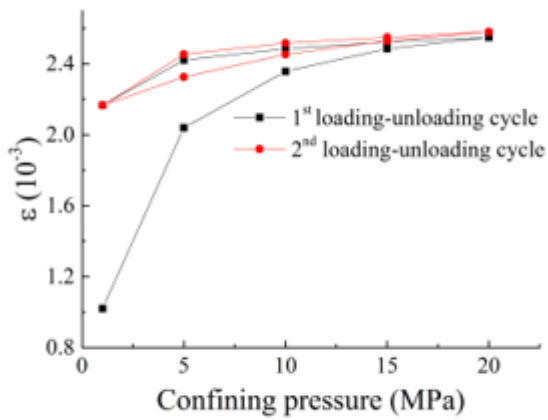
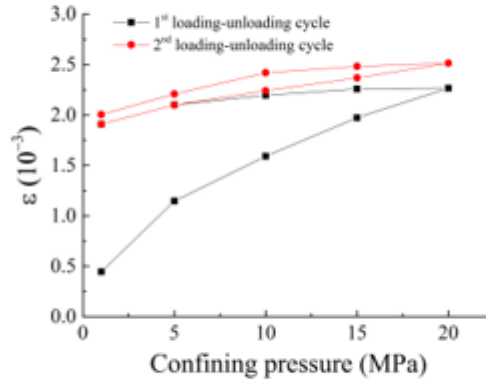


Figure 4

Effect of confining pressure on gas permeability of (a) sample C-1 and (b) C-2;



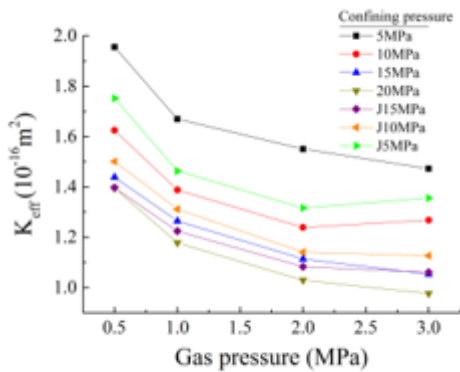
(a)



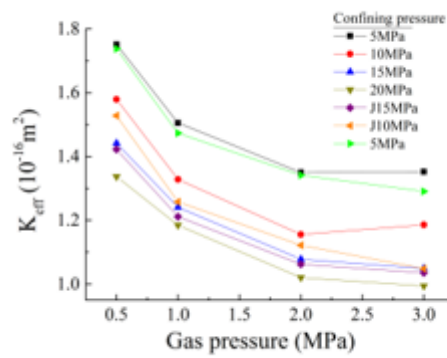
(b)

Figure 5

Effect of confining pressure on deformation of sandstone ($P_g=0.5$ MPa) (a) sample C-1 and (b) sample C-2.



(a)



(b)

Figure 6

(second Figure 5) Effect of gas pressure on the gas permeability during (a) the 1st loading-unloading phase; (b) the 2nd loading-unloading phase.

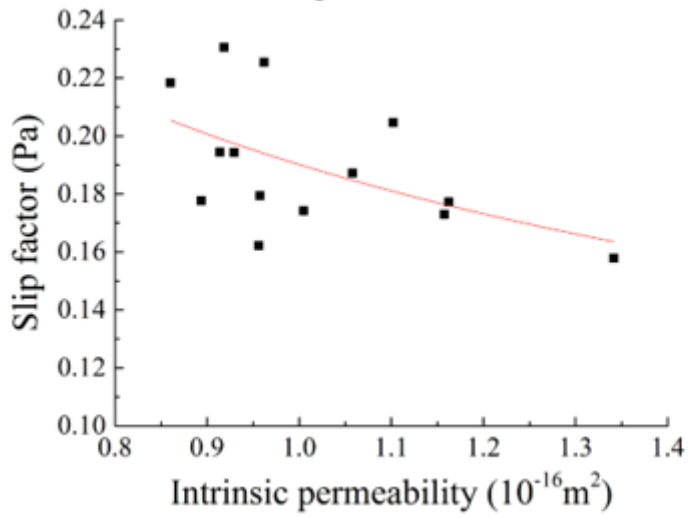


Figure 7

Linear Klinkenberg relationship for the sample. (Figure 6)

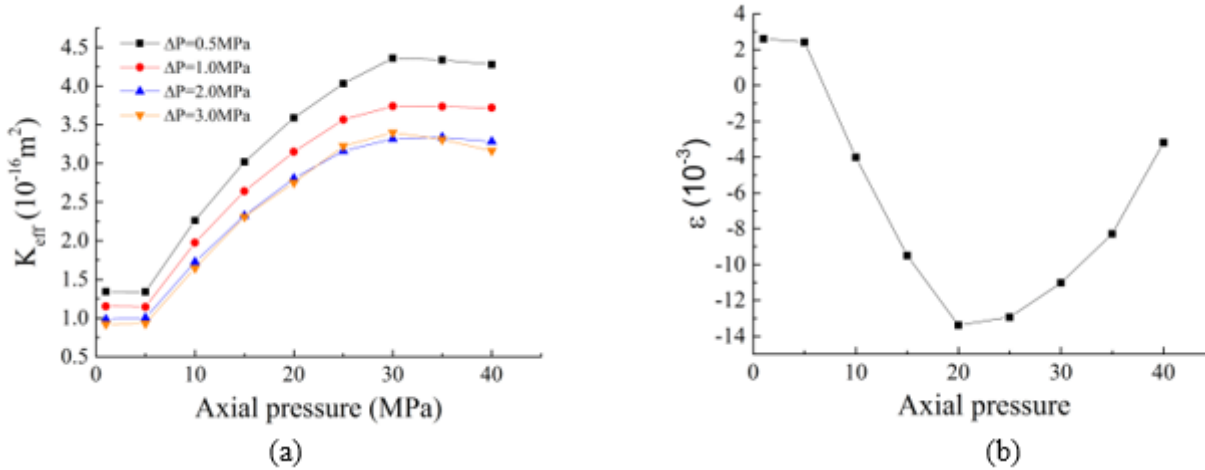


Figure 8

(third Figure 5) Effect of axial pressure on (a) gas permeability; (b) deformation.

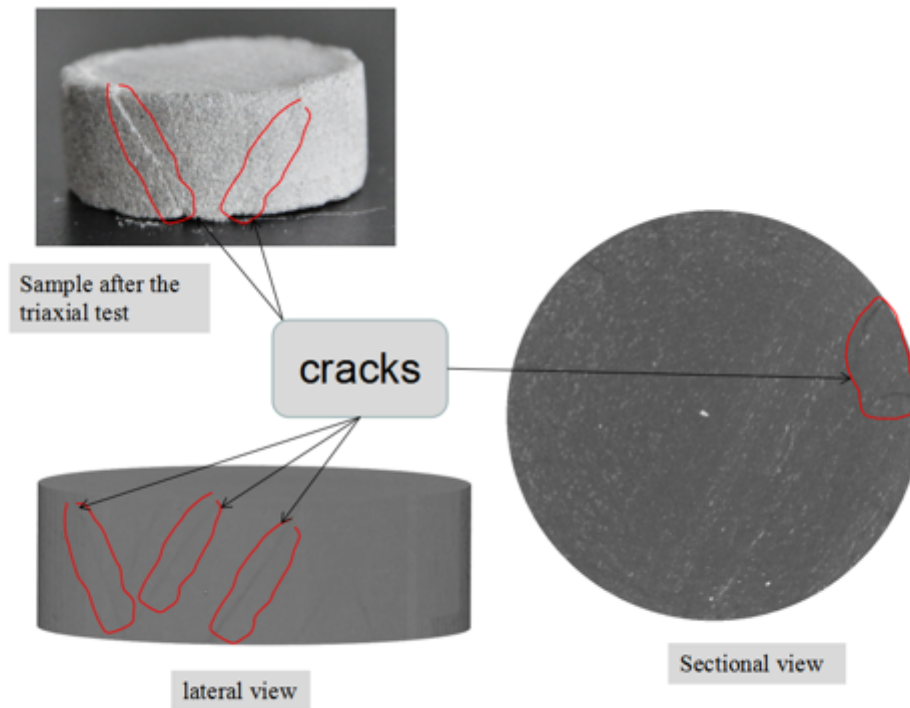


Figure 9

(second Figure 6) 3D reconstruction model (3D X-ray) of sandstone after the end of the gas permeability test.

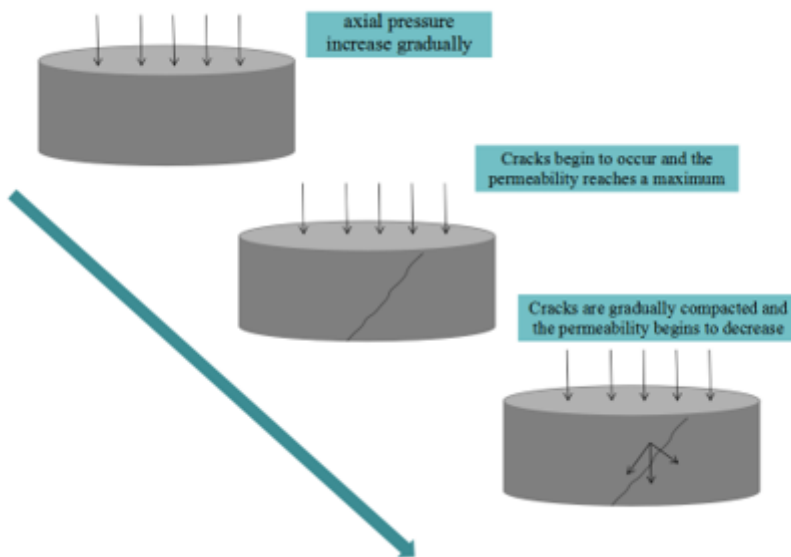


Figure 10

Schematic diagram of the crack development and permeability evolution under triaxial conditions. (Figure 7)

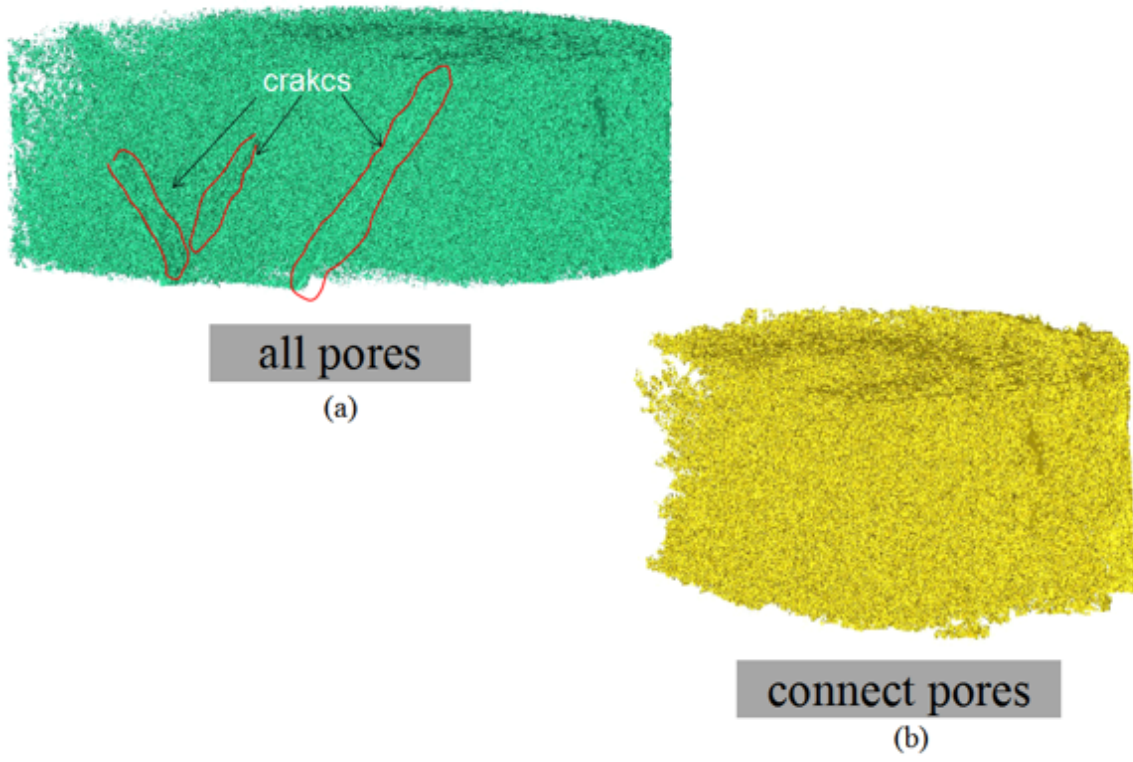


Figure 11

(a) Pore network of sandstone; (b) the interconnected pore network of sandstone. (Figure 8)